This article was downloaded by:
On: *29 January 2011*
Access details: *Access Details: Free Access*
Publisher *Taylor & Francis*
Informa Ltd Registered in England and Wales Registered Number: 1072954 Registered office: Mortimer House, 37-41 Mortimer Street, London W1T 3JH, UK

Supramolecular Chemistry
Publication details, including instructions for authors and subscription information:
http://www.informaworld.com/smpp/title~content=t713649759

Metallosupramolecular Chemistry in Two Dimensions

Markus Schütte; Christa Stolle; Dirk G. Kurth

Online publication date: 13 May 2010

To cite this Article Schütte, Markus , Stolle, Christa and Kurth, Dirk G.(2003) 'Metallosupramolecular Chemistry in Two Dimensions', Supramolecular Chemistry, 15: 7, 549 — 555
To link to this Article: DOI: 10.1080/1061027031000160513 3
URL: http://dx.doi.org/10.1080/10610270310001605133

PLEASE SCROLL DOWN FOR ARTICLE

Full terms and conditions of use: http://www.informaworld.com/terms-and-conditions-of-access.pdf

This article may be used for research, teaching and private study purposes. Any substantial or systematic reproduction, re-distribution, re-selling, loan or sub-licensing, systematic supply or distribution in any form to anyone is expressly forbidden.

The publisher does not give any warranty express or implied or make any representation that the contents will be complete or accurate or up to date. The accuracy of any instructions, formulae and drug doses should be independently verified with primary sources. The publisher shall not be liable for any loss, actions, claims, proceedings, demand or costs or damages whatsoever or howsoever caused arising directly or indirectly in connection with or arising out of the use of this material.

Supramolecular Chemistry, 2003 Vol. 15 (7–8), pp. 549–555

Taylor & Francis
Taylor & Francis Group

Metallosupramolecular Chemistry in Two Dimensions

MARKUS SCHÜTTE, CHRISTA STOLLE and DIRK G. KURTH*

Max Planck Institute of Colloids and Interfaces, Research Campus Golm, D-14424 Potsdam, Germany

Received 21 October 2002; Accepted 4 December 2002

Ultrathin films of metallosupramolecular coordination polyelectrolytes (MEPEs) on planar solid substrates assembled by electrostatic layer-by-layer self-assembly (ELSA) are characterized with UV-vis spectroscopy, optical ellipsometry, and X-ray reflectometry. MEPEs based on different ditopic ligands and transition metal ions are employed and shown to form regular ELSA multilayers. A quantitative analysis is in agreement with a surface coverage of approximately two MEPE monolayers per deposition step. In addition, we demonstrate that multilayers of MEPEs with different transition metal ions can be assembled. Even with kinetically labile metal ions, there is no metal ion exchange in these multilayers. Absorption spectra of multilayers on silicon show a band inversion of the MLCT band, which is rationalized in terms of optical effects.

Keywords: Electrostatic layer-by-layer self-assembly; Thin films; Supramolecular chemistry; Metallosupramolecular coordination polyelectrolytes; Materials

INTRODUCTION

Molecular self-organization, a universal driving force in nature, represents a rational approach to combine,

Downloaded At: 15:20 29 January 2011

The Future of Supramolecular Chemistry

Intelligent and dynamic systems are one of the next frontiers in supramolecular chemistry. For the realization of such materials, it will be necessary to improve existing methods and to innovate new routes to organize supramolecular modules in structurally coherent macroscopic architectures. In analogy to biological systems, semi-ordered mesoscopic materials will become increasingly important. Applying principles of self-organization in device fabrication provides opportunities that go far beyond currently existing technologies and will have a profound impact on the technological development far into the 21st century. However, further progress in this area will rely on an interdisciplinary approach. In this sense, the visionary claims of a supramolecular paradigm may provide an incentive to combine forces towards interdisciplinary research programs that go beyond "classical" approaches in chemistry, engineering, or physics.

D. G. Kurth studied chemistry at the University of Cologne, the Technical University of Aachen, the University of New Mexico, and Purdue University. After he finished his PhD in the group of T. Bein, he went as post-doc to Strasbourg to work with J.-M. Lehn. Since 1996, he has been an independent project leader in the Department of Interfaces headed by H. Möhwald at the Max Planck Institute of Colloids and Interfaces at Potsdam.

*Corresponding author. Tel.: +49-331-567-9211. Fax: +49-331-567-9202. E-mail: kurth@mpikg-golm.mpg.de

ISSN 1061-0278 print/ISSN 1029-0478 online © 2003 Taylor & Francis Ltd
DOI: 10.1080/1061027031000160513

position, and orient molecular components in well-defined architectures through weak non-covalent interactions. Through a sequence of recognition, growth and termination steps, the supramolecular modules (SUMOs) emerge spontaneously from suitably instructed components [1]. Intriguing examples of SUMOs have been reported, exploiting ligand–metal ion coordination [2], π–π interactions [3], or hydrogen-bonding [4,5]. The modularity of self-assembly provides access to a wide range of structures and functions and permits control thereof from molecular to macroscopic length scales. The ability of SUMOs to accomplish intricate functions provides opportunities that go far beyond current micro-fabrication technology [6]. Applications of such systems are intriguingly diverse, including information storage, signal transduction and amplification, as well as host–guest recognition [7].

While the principles that govern self-assembly are well developed, the integration of SUMOs into a device or a material is the next challenge. Material and device performance is critically dependent on the spatial arrangements of the functional modules [8,9]. Controlling the correlation of position and orientation of the modules in the final architecture is crucial for full exploitation of a material's potential and the encoding of new (collective) properties. An ultimate goal is, therefore, to exploit principles of molecular self-organization in device fabrication to overcome some of the intrinsic problems associated with conventional lithography technology: parallel fabrication, (molecular) dimension control, component alignment, and repair mechanisms as in biological systems. Here, existing methods have to be improved, and new routes have to be innovated to redeem the visionary pledges of supramolecular systems.

However, the integration of SUMOs in complex architectures gives rise to another problem. The potential lack of symmetrical invariance (e.g. crystallinity) in supramolecular devices and materials poses a serious challenge to structure determination by traditional diffraction methods, which is of prime importance for the understanding of structure–property relationships. The full scope of this problem becomes apparent if we consider biological systems. These mostly mesoscopic systems with order at short- or intermediate-length scales exhibit an enormous wealth of functional properties. Applying this lesson from nature to the design of novel materials implies that semi-ordered structures will become increasingly important, which consequently calls for corresponding developments in analytical sciences.

Metallosupramolecular modules (MEMOs) originating from metal-ion-directed self-assembly are of particular interest for the construction of functional devices [10]. They provide a set of well-defined coordination geometries, a range of binding strengths and ligand exchange kinetics that allow reversible assembly–disassembly of supramolecular architectures, including switchable interaction sites, e.g. electrochemical interconversion between redox states of different coordination geometries. In addition, they possess a variety of photochemical, electrochemical, and reactive properties that are relevant for functional devices. In principle, it is, therefore, possible to tailor the thermodynamic, kinetic, and functional properties of these devices by the judicious choice of metal ions and ligands.

Owing to the numerous properties of MEMOs, one can envision a wide variety of potential applications that utilize photons, electrons, spin transitions, and recognition phenomena to store and process information. Strong absorption, high quantum yields, suitable excited state lifetimes, and luminescence make MEMOs promising candidates as components in photonic devices. The optical absorption bands are often associated with large optical non-linearities. Tunable redox states and a reversible electrochemistry of metal ion complexes open interesting perspectives for electronic applications. Through the coordination geometry of the central metal ion, it is possible to introduce chirality that in turn can be utilized in molecular recognition or to generate materials with non-centrosymmetric space groups. While photo-mediated charge separation in polynuclear complexes [11] has been studied in terms of artificial photosynthesis, such systems are also interesting for information-processing devices. The importance of transition metal ion complexes as components in molecular-based, photoreactive devices and materials becomes apparent in effects like light-induced excited spin state trapping (LIESST) [12], reverse LIESST [13] and low spin (LS) LIESST [14] effects, metal-to-ligand charge transfer in nitroprusside [15], metal-to-metal charge transfer as in Prussian blue analogues [16], valence tautomerism of catecholate ligands in Co(II) complexes [17], as well as ligand-driven light-induced spin-state change (LD-LISC) [18].

With the recent discovery of metallosupramolecular coordination polyelectrolytes (MEPEs) [19] based on ditopic bis-terpyridines and their corresponding polyelectrolyte–amphiphile complexes (PACs) [20], model systems are now available that provide a facile entry towards fabricating hierarchical architectures, including nanostructures [21], Langmuir monolayers [22,23] and Langmuir–Blodgett multilayers [24], thin films [19], capsules [25,26], and mesophases [27]. It is well established by now that electrostatic layer-by-layer self-assembly (ELSA) of MEPEs with oppositely charged polyelectrolytes results in multilayers (Scheme 1). Here, we describe the fabrication and characterization of such multilayers with MEPEs based on

Downloaded At: 15:20 29 January 2011

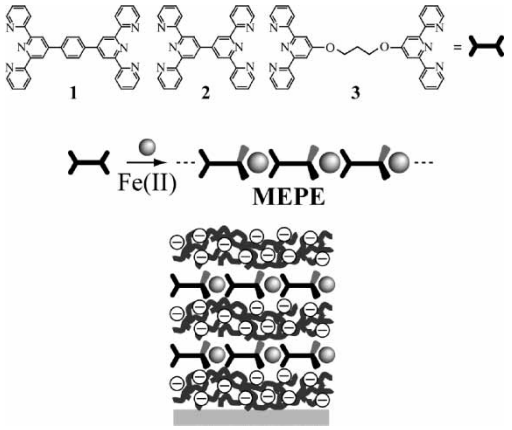

SCHEME 1 Metal-ion coordination of ditopic bis-terpyridine ligands such as **1**, **2**, and **3** resulting in the spontaneous formation of linear metallosupramolecular coordination polyelectrolytes (MEPE). The octahedral coordination geometry around the transition metal ion is indicated by the wedges. Electrostatic layer-by-layer self-assembly of the positively charged MEPEs with oppositely charged polyelectrolytes, such as polystyrenesulfonate, provides a route to implement MEMOs in ultrathin multilayers.

different ditopic ligands and metal ions as well as mixed MEPE multilayers. Multilayers consisting of different MEPEs with distinct redox characteristics can give rise to vectorial properties such as charge or electron transfer, which is of importance for rectification and photovoltaic devices.

RESULTS AND DISCUSSION

UV-vis absorption spectroscopy is very useful for the characterization of MEPE multilayers because it provides qualitative as well as quantitative information and is very sensitive and easy to use. Strong $\pi-\pi^*$ transitions in the range of 260–350 nm and metal-to-ligand charge-transfer (MLCT) bands at around 600 nm as well as weaker d–d transitions above 350 nm make MEPEs ideal candidates for this technique. UV-vis spectra of Fe(II)-MEPE-**2**, Ni(II)-MEPE-**2** and Ni(II)-MEPE-**3** multilayers with PSS on quartz is shown in Fig. 1 [28]. In both cases, a regular increase in the absorption intensity indicates layer-by-layer growth. The absorbance at selected wavelengths as a function of the number of layers is shown in the inserts confirming linear growth. The straight lines do not pass through the origin because the amount adsorbed in the first step is somewhat smaller, as in consecutively deposited layers, which is possibly due to a substrate effect. The surface coverage, Γ, can be determined from the absorption intensity, A_λ, and the extinction coefficient, ε_λ, at wavelength λ by $\Gamma = [A_\lambda N]/2\varepsilon_\lambda$. Here, two effects have to be considered. First, the band contour is dependent on the local environment, and, second, optical effects in thin films such as reflection losses

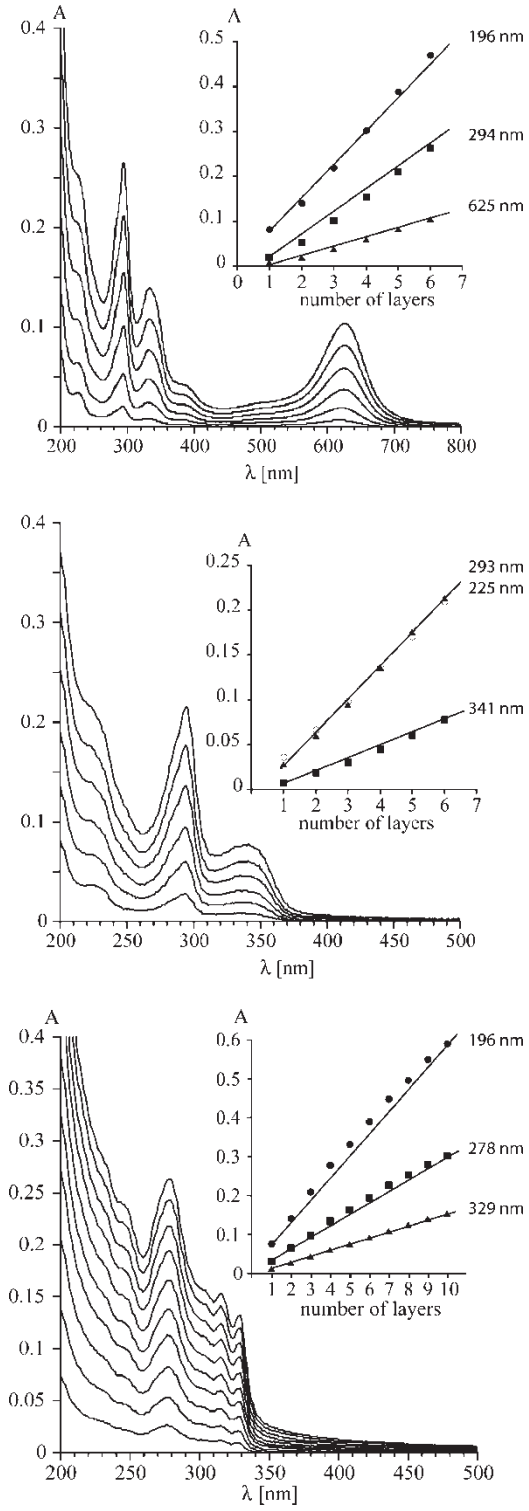

FIGURE 1 UV-vis spectra of multilayers of Fe(II)-MEPE-**2** (top), Ni(II)-MEPE-**2** (middle), and Ni(II)-MEPE-**3** assembled with PSS as a function of the layer numbers. The insets show absorbance maxima at selected wavelengths confirming linear growth in all cases.

can contribute to the adsorption. Therefore, this analysis provides only an estimate for the surface coverage. The average absorption at 294 nm (625 nm) is 0.28 (0.11) (films on both sides of the substrate),

Downloaded At: 15:20 29 January 2011

and the surface coverage amounts to 2.4 and 2.0 chromophores per nm^2 [29]. The area of ligand **2** is estimated to be approximately 1.4 nm^2. If we assume that the chromophores in the multilayer are oriented with the long axis parallel to the substrate, the surface coverage corresponds to approximately three molecular layers. If, in addition, the anisotropy is taken into account, the surface coverage corresponds to approximately two molecular strata [30]. Depending on the packing, the thickness is estimated to be 1.8–2.4 nm (*vide infra*). Similar values are obtained for the surface coverage of Ni(II)-MEPE-**2**. These results are in agreement with previously published data [31].

While ELSA is readily applied to MEPEs assembled from different ligands and metal ions, an important consideration is whether different MEPEs can be incorporated in the same multilayer without exchange or loss of metal ions. In Fig. 2, UV-vis spectra of Fe(II)-MEPE-**1** and Ni(II)-MEPE-**1** in different multilayer architectures are shown. In the first case, three layers of Ni(II)-MEPE-**1** and PSS are assembled, followed by three layers of Fe(II)-MEPE-**1** and PSS. The increase in the absorption bands in the range of 250–400 nm, which are associated with $\pi-\pi^*$ transitions of the ligand, as shown in the inset, clearly confirms overall linear growth. The absorption of the MLCT band of Fe(II)-MEPE-**1** is 0.019 per layer [19]. Therefore, we expect a total absorbance of approximately 0.06 for three layers, which is exactly what is determined experimentally. From the total intensity of the MLCT band, we conclude that no exchange of Ni(II) occurs during ELSA as Fe(II)-MEPE-**1** is assembled on top of the Ni(II)-MEPE-**1**/PSS layer. Similarly, if first three layers of Fe(II)-MEPE-**1**/PSS are deposited, followed by three layers of Ni(II)-MEPE-**1**/PSS, there is no significant loss in the band intensity of the MLCT transition (Fig. 2, middle). The steady increase in the absorption intensity in the 250–350 nm range confirms linear multilayer growth, while the MLCT band at 591 nm confirms that Fe(II) fully remains in the bottom layer. In the case of alternate deposition of Fe(II)-MEPE-**1** and Ni(II)-MEPE-**1**, we also observe overall linear growth with no sign of metal-ion exchange. A comparison of the absorbance intensities of the different layer architectures underlines the fidelity of multilayer formation. These results demonstrate that different MEPEs can be assembled in mutlilayers, even with kinetically labile transition-metal ions without any significant loss or exchange of metal ions.

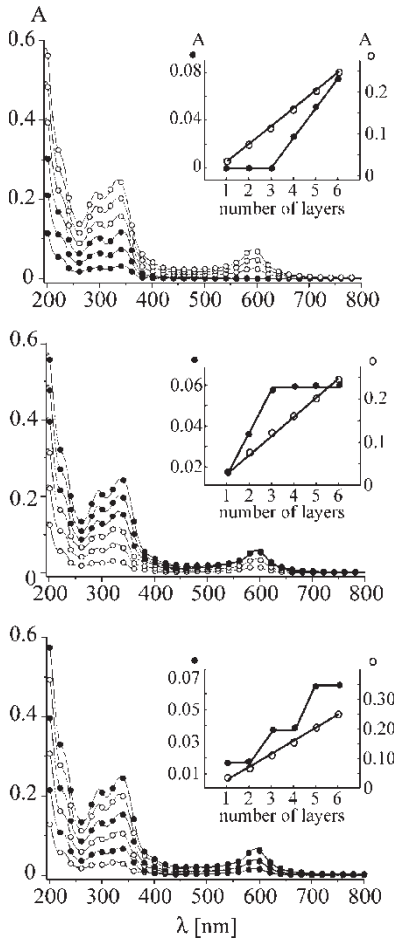

FIGURE 2 UV-vis spectra of MEPE/PSS multilayers with different architectures. Top: $[Ni(II)\text{-MEPE-}\mathbf{1}/PSS)_3(Fe(II)\text{-MEPE-}\mathbf{1}/PSS]_3$. Middle: $[Fe(II)\text{-MEPE-}\mathbf{1}/PSS)_3(Ni(II)\text{-MEPE-}\mathbf{1}/PSS]_3$. Bottom: $[Fe(II)\text{-MEPE-}\mathbf{1}/PSS/Ni(II)\text{-MEPE-}\mathbf{1}/PSS]_3$. The progression of the MLCT band (inset, filled circles) shown in the insets shows that there is no loss of or exchange of metal ions during ELSA. The increase in the absorption bands associated with $\pi-\pi^*$ transitions in the region from 250 to 350 nm (inset, open circles) moreover confirms linear growth.

Silicon wafers play an important role in device fabrication, and they are also advantageous for certain analytical methods such as atomic force microscopy. Therefore, we investigate ELSA on silicon using UV-vis spectroscopy in reflection, optical ellipsometry, and X-ray reflectometry (XRR). The UV-vis spectra of Fe(II)-MEPE-**1**/PSS multilayers on silicon are shown in Fig. 3. In the following, we will focus on the MLCT band at around 600 nm. As one can see, the band intensity is inversed in this region of the UV-vis spectrum. The reason for this is an optical effect originating from the contribution of the anomalous dispersion to the reflection of the Si-multilayer interface. Compared with transmission spectra, optical effects in reflection spectra can cause band shifts, asymmetries, splitting and distortions. To verify this hypothesis, we need to compute reflectance spectra based on a classical electrodynamic theory approach. To do so, we need the optical response function that is the wavelength-dependent complex refractive index of bulk Fe(II)-MEPE-**1** as well as an accurate film thickness of the multilayer.

A comparison of UV-vis spectra of Fe(II)-MEPE-**1** in solution and of a $[Fe(II)\text{-MEPE-}\mathbf{1}/PSS]_{10}$ multilayer on quartz reveals that the spectroscopic

Downloaded At: 15:20 29 January 2011

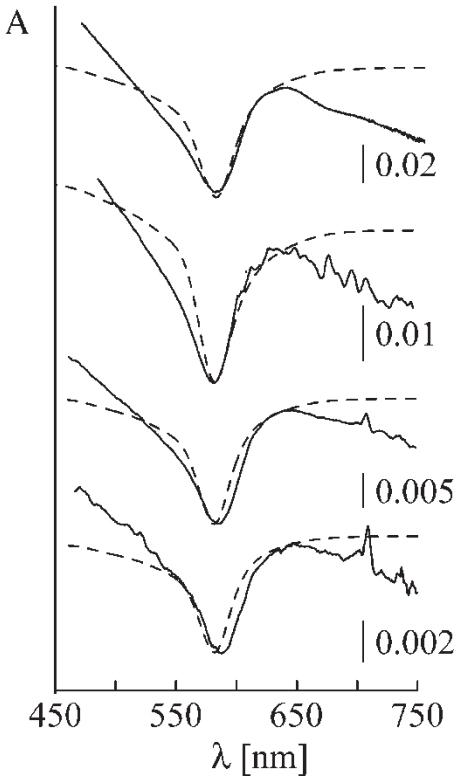

FIGURE 3 Reflection–absorption UV-vis spectra of multilayers assembled on silicon wafers with the composition Si/PEI/PSS[Fe(II)-MEPE-**1**/PSS]$_n$, with $n = 1$, 3, 5, and 10 (bottom to top). The dotted lines show the calculated reflectance curves. The agreement between computed and experimental spectra in terms of band position and shape confirms the contribution of optical effects to the reflection–absorption spectra resulting in a band inversion of the MLCT band.

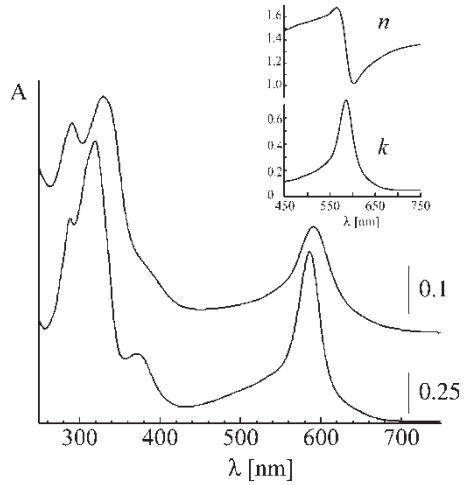

FIGURE 4 Transmission UV-vis spectra of Fe(II)-MEPE-**1** in solution (bottom) and of a multilayer on quartz (top) with the composition PEI/PSS[Fe(II)-MEPE-**1**/PSS]$_{10}$. The inset shows the real (n) and imaginary (k) part of the complex refractive index of the MLCT band obtained from the transmission solution spectrum and a Kramers–Kronig transformation.

signature of Fe(II)-MEPE-**1** remains mainly unaltered in the multilayer (Fig. 4). The slight shifts in band positions are attributed to differences in the local environment in the film compared with the solution. The qualitative agreement of the spectra indicates that we can use the complex refractive index determined from the solution UV-vis spectrum (see inset Fig. 4) to compute the corresponding reflection spectrum.

Next, we determine the thickness of the multilayers using a combined approach of optical ellipsometry and XRR. Figure 5 shows the experimental X-ray reflectance curve (triangles) and the computed reflectance curve (solid line) of a multilayer composed of Si/PEI[PSS/Fe(II)-MEPE-**1**]$_5$PSS. The inset shows the plot of the order of interference, m, vs. the angle of incidence, ϕ_0. An analysis of the Kiessig fringes gives a thickness of 19.1 nm, while the computed reflectance curve (solid line) provides a value of 19.3 nm. This comparison shows that the assumptions and parameters in the underlying model used to compute the reflectance curves are correct. The average layer thickness, therefore, amounts to approximately 17 Å if we assume a thickness of 5 Å for the PEI adhesion layer. The lateral extension of Fe(II)-MEPE-**1** is estimated to be 12 Å, so the thickness corresponds to one to two layers, which is consistent with the UV-vis measurements (*vide supra*).

While the Kiessig analysis is simple and parameter-free, computing and fitting the reflectance curve also provides the roughness and the electron density. The total interfacial roughness is determined to be 0.4 nm, in agreement with the occurrence of more than 10 distinct interference fringes. It is interesting to note that the interfacial roughness is

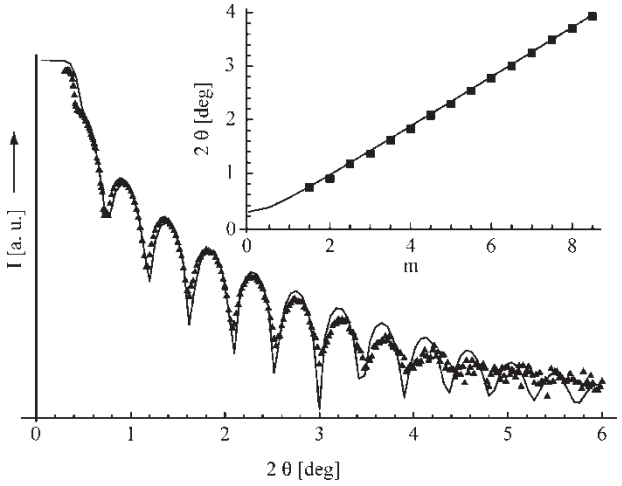

FIGURE 5 Experimental (triangles) and calculated (solid line) X-ray reflectance data for a ELSA multilayer with the composition Si/PEI[PSS/Fe(II)-MEPE-**1**]$_5$PSS. The following parameters are used for the computation: electron densities multilayers (1) and silicon (2): δ_1 3 10^{-6}, δ_2 7 10^{-6}, β_2 4 10^{-7}, interfacial roughness 0.4 nm, thickness 19.3 nm. The inset shows a plot of the order of interference, m, vs. the angle of incidence, ϕ_0. The first observable extremum occurs at $m = 3/2.1$.

Downloaded At: 15:20 29 January 2011

much smaller than the dimension of the macromolecular components. The absence of Bragg reflections in the reflectance curve further suggests that the layers are not stratified. Most likely, interpenetration of the polyelectrolytes results in a homogeneous electron density through the film. Similar results on the film thickness are obtained by optical ellipsometry. The agreement of ellipsometry and XRR data confirm that proper optical constants are used to describe the interface including electron density and refractive index.

Finally, we can compute the reflectance spectra based on the experimentally determined refractive index and the film thickness. A comparison of the experimental and calculated spectra in Fig. 3 shows that the computed reflectance spectra describe the band inversion in terms of the band position, intensity, and shape quite accurately. Deviations are expected because the samples include spectral contributions from the PSS layers that are not accounted for in the refractive index used for the calculation. Similarly, the complex refractive index of silicon varies considerably in the UV-vis region and assumes a real constant value only above 500 nm [32]. For these reasons, the computed reflectance curves were limited to the MLCT region in the visible range of the spectrum.

From the above analysis, it becomes clear that the band inversion seen in reflection spectra on silicon wafers is a purely optical effect. The reason for this effect is that the imaginary part of the complex refractive index of Fe(II)-MEPE-**1** ($k = 0.07$) exceeds that of silicon ($k = 0.025$) within the MLCT band. As a result, more radiation at that wavelength is reflected towards the detector compared with the blank silicon reference wafer. It is expected that spectra of MEPEs with transition metal ions that show similar absorption bands in the vis-range, such as Ru, will also exhibit band distortions.

MATERIALS AND METHODS

The synthesis of the materials, electrostatic layer-by-layer self-assembly, as well as the methods and instruments are described in previous publications [19,33]. UV-vis reflection spectra on commercial silicon wafers were recorded with a Cary 400 spectrophotometer and a commercial Cary reflection accessory with a constant angle of incidence of 7°. Fe(II)-MEPE-**1**. UV-vis (methanol): λ_{max} (ε in cm^2 $mmol^{-1}$) = 287 (42,500), 322 (57,900), 585 (30,000). Ni(II)-MEPE-**1**. UV-vis (methanol): λ_{max} (ε in cm^2 $mmol^{-1}$) = 294 (32,160), 334 (35980), 340 (36,560), 438 (1000). Fe(II)-MEPE-**2**. UV-vis (methanol): λ_{max} (ε in cm^2 $mmol^{-1}$) = 293 (58,240), 327 (27,490), 382 (7830), 631 (27,630).

The wavelength-dependent complex index of refraction, $N(\lambda) = n(\lambda) - ik(\lambda)$, of Fe(II)-MEPE-**1** is obtained as follows. The imaginary part is obtained from a transmission absorbance spectrum according to

$$k = \frac{\lambda\delta}{5.46AczM}$$

where c is the concentration, δ is the density and M is the molar mass of the analyte, λ is the wavelength, z is the path length of the cell, and A is the experimentally determined absorbance [34]. For brevity, constant factors are lumped into a single number. The real part of the complex refractive index is obtained by a Kramers–Kronig transformation of the k spectrum according to

$$n(\nu_o) = n_\infty + \frac{2P}{\pi}\int \frac{\nu k(\nu)}{\nu^2 - \nu_o^2}\,d\nu$$

where ν equals $1/\lambda$, n_∞ is the refractive index far away from any absorption band, and P denotes the principal value of the integral [35]. UV-vis reflectance spectra were calculated by classical electrodynamic theory using the Fresnel reflection coefficients [36–38]. XRR data were evaluated by the Kiessig method [39] as well as by a fitting procedure [40,41]. For ellipsometry, the imaginary refractive index at 633 nm determined from UV-vis spectroscopy was used. A real index of refraction, n, of 1.5 was used. A variation of n from 1.45 to 1.55 does not significantly affect the computed film thickness [42]. Owing to model and experimental errors, the computed thickness is a complex number. The real part of this complex value was taken as the film thickness. The imaginary part, which can be interpreted as an estimate of errors, is typically smaller than 10% of the real part of the complex thickness.

Acknowledgements

The authors thank Helmuth Möhwald for valuable discussions. Financial support by Deutsche Forschungsgemeinschaft (DFG) is greatly appreciated.

References

[1] Lehn, J.-M. *Supramolecular Chemistry—Concepts and Perspectives*; VCH-Wiley: Weinheim, 1995.
[2] Stang, P. J.; Olenyuk, B. *Acc. Chem. Res.* **1997**, *30*, 502–518.
[3] Claessens, C. G.; Stoddart, J. F. *J. Phys. Org. Chem.* **1997**, *10*, 254–272.
[4] Whitesides, G. M.; Simanek, E. E.; Mathias, J. P.; Seto, C. T.; Chin, D.; Mammen, M.; Gordon, D. M. *Acc. Chem. Res.* **1995**, *28*, 37–44.
[5] Rebek, J. *Acc. Chem. Res.* **1999**, *32*, 278–286.
[6] Kurth, D. G. *Ann. N. Y. Acad. Sci.* **2002**, *960*, 29–38.
[7] Balzani, V.; Credi, A.; Raymo, F. M.; Stoddart, J. F. *Angew. Chem., Int. Ed.* **2000**, *39*, 3348–3391.
[8] Krass, H.; Plummer, E. A.; Haider, J. M.; Barker, P. R.; Alcock, N. W.; Pikramenou, Z.; Hannon, M. J.; Kurth, D. G. *Angew. Chem.* **2001**, *113*, 3980–3983.

Downloaded At: 15:20 29 January 2011

[9] Krass, H.; Plummer, E. A.; Haider, J. M.; Barker, P. R.; Alcock, N. W.; Pikramenou, Z.; Hannon, M. J.; Kurth, D. G. *Angew. Chem., Int. Ed.* **2001**, *40*, 3862–3865.
[10] Constable, E. C. *Electronic Materials: The Oligomer Approach*; VCH-Wiley: Weinheim, 1998.
[11] Balzani, V.; Scandola, F. *Supramolecular Photochemistry*; Ellis Horwood: New York, 1991.
[12] Decurtins, S.; Gütlich, P.; Kohler, C. P.; Spiering, H.; Hauser, A. *Chem. Phys. Lett.* **1984**, *105*, 1.
[13] Decurtins, S.; Gütlich, P.; Hasselbach, K. M.; Hauser, A.; Spiering, H. *Inorg. Chem.* **1985**, *24*, 2174.
[14] Renz, F.; Osio, H.; Ksenofontov, V.; Waldeck, M.; Spiering, H.; Gütlich, P. *Angew. Chem., Int. Ed.* **2000**, *39*, 3699.
[15] Gu, Z. Z.; Sato, O.; Iyoda, T.; Hashimoto, K.; Fujishima, A. *J. Phys. Chem.* **1996**, *100*, 18289.
[16] Sato, O.; Iyota, A.; Fujishima, A.; Hashimoto, K. *Science* **1996**, *272*, 704.
[17] Attia, A. S.; Jung, O. S.; Pierpont, C. G. *Inorg. Chim. Acta* **1994**, *226*, 91.
[18] Boillot, M.-L.; Roux, C.; Audiere, J.-P.; Dausse, A.; Zarembowitch, J. *Inorg. Chem.* **1996**, *35*, 3975.
[19] Schütte, M.; Kurth, D. G.; Linford, M. R.; Cölfen, H.; Möhwald, H. *Angew. Chem., Int. Ed.* **1998**, *37*, 2891–2893.
[20] Kurth, D. G.; Lehmann, P.; Schütte, M. *Proc. Natl Acad. Sci. USA* **2000**, *97*, 5704–5707.
[21] Kurth, D. G.; Severin, N.; Rabe, J. *Angew. Chem., Int. Ed.* **2002**, *114*, 3681–3683.
[22] Lehmann, P.; Kurth, D. G.; Brezesinski, G.; Symietz, C. *Chem. Eur. J.* **2001**, *7*, 1646–1651.
[23] Khattari, Z.; Hatta, E.; Kurth, D. G.; Fischer, T. M. *J. Chem. Phys.* **2001**, *115*, 9923–9928.
[24] Bodenthin, Y.; Grenzer, J.; Lauter, R.; Pietsch, U.; Lehmann, P.; Kurth, D. G.; Möhwald, H. *J. Synchrotron Radiat.* **2002**, *9*, 206–209.
[25] Kurth, D. G.; Caruso, F.; Schüler, C. *Chem. Commun.* **1999**, 1579–1580.
[26] Caruso, F.; Schüler, C.; Kurth, D. G. *Chem. Mater.* **1999**, *11*, 3394–3399.
[27] Kurth, D. G., Meister, A., Förster, G., Thünemann, A. *Langmuir* **2003**, *19*, 4055–4057.
[28] In this nomenclature, the prefix indicates the central metal ion, and the final number indicates the type of ligand used.
[29] The fact that the surface coverage at 294 nm is larger than at 624 nm is attributed to a stronger reflection loss at this wavelength due to the strong dispersion in this part of the spectrum.
[30] Kurth, D. G.; Schütte, M.; Wen, J. *Colloid Surf. A-Physicochem. Eng. Asp.* **2002**, 198–200, 633–643.
[31] Kurth, D. G.; Osterhout, R. E. *Langmuir* **1999**, *15*, 4842–4846.
[32] Palik, E. D. *Handbook of Optical Constants of Solids*; Academic Press: New York, 1985.
[33] Kurth, D. G.; Schütte, M. *Macromol. Symp.* **2001**, *164*, 167–179.
[34] Stone, J. M. *Radiation and Optics*; McGraw-Hill: New York, 1965.
[35] Kurth, D. G.; Bein, T. *Langmuir* **1995**, *11*, 578–584.
[36] Kang, J. F.; Ulman, A.; Jordan, R.; Kurth, D. G. *Langmuir* **1999**, *15*, 5555–5559.
[37] Parikh, A. N.; Allara, D. L. *J. Phys. Chem.* **1992**, *96*, 927–945.
[38] Born, M.; Wolf, E. *Principles of Optics*; Pergamon: Oxford, 1993.
[39] Kiessig, H. *Annalen der Physik* **1931**, *5*, 769–788.
[40] Asumssen, A.; Riegler, H. *J. Chem. Phys.* **1996**, *104*, 8159–8164.
[41] Russel, T. P. *Mater. Sci. Rep.* **1990**, *5*, 171–271.
[42] Kurth, D. G.; Bein, T. *Langmuir* **1995**, *11*, 3061–3067.

Downloaded At: 15:20 29 January 2011